Influence of Microstructure on the Compressive Response of Filament-Wound Carbon Fiber/Epoxy Composite Tubes

I. Shola-Shittu[1], and J. Montesano[1] *

[1] Composites Research Group, Department of Mechanical and Mechatronic Engineering, University of Waterloo, Waterloo, Canada

* *Corresponding author (john.montesano@uwaterloo.ca)*

Keywords: *Filament Winding; Carbon Fiber/Epoxy Composite; Microstructural Characterization; Mechanical Testing.*

1. Abstract

This study investigates the relationship between the microstructure and compressive response of towpreg-based filament-wound carbon fiber/epoxy composite tubes. Cross-sectional and longitudinal samples are assessed via optical microscopy, and full cylindrical tubular specimens with nominal winding angles of ±10° and ±45° are tested in axial compression. Microscopy of the ±45° tubes shows low measured void content but clear tow-scale geometric variability, including nonuniform height, tow overlaps, and resin-rich regions. The ±10° tubes exhibited similar microstructure variability and more pronounced defects. Initial compression results for ±45° specimens show distinct peak compressive stresses of 79.94 MPa and 59.27 MPa. Full-field strain measurements using digital image correlation reveal that both specimens develop narrow 45°-aligned strain localization bands, while one specimen exhibits a measurable nonlinear regime prior to localization and the other transitions more directly from elastic response to damage development. These results provide an initial process-structure-property relationship for compression-loaded filament-wound composite tubes.

2. Introduction

Filament winding remains one of the most established and suitable automated composite manufacturing processes for axisymmetric composite structures such as tubes, cylinders, pressure vessels, and shafts because it enables continuous fiber placement along prescribed load paths with efficient material utilization [1], [2]. In recent years, renewed interest in this process has developed, not only because of the high demand for lightweight structural components in aerospace and energy applications such as hydrogen storage tanks, but also by the increasing use of towpreg, which improves process cleanliness and resin-content control relative to conventional wet winding. Towpreg offers superior control over the resin-to-fiber ratio, and can reduce void content to approximately 2%, compared to the 6% typically found in wet winding [3]. When coupled with advanced computer-controlled automation, filament winding processes utilizing towpreg can yield parts with repeatable quality and winding pattern [3].

Despite these advantages, the automated placement of tows in helical patterns creates a complex "pseudo-woven" architecture characterized by fiber crossovers and undulations (i.e., fiber curvature), where the severity is dependent on the winding angle. While these features are intrinsic to the filament winding process, they deviate significantly from the idealized unidirectional laminate assumptions often used in predictive modeling of the mechanical behavior of filament-wound composite tubes [4]. Real filament-wound material architectures contain process-induced microstructural features such as tow undulations, an interlaced tow mosaic pattern, tow overlaps, resin-rich regions, and voids, all of which can influence local deformations and stress fields and failure initiation [5], [6], [7], [8]. Recent studies have shown that winding patterns affect the response of wound cylinders and tubes under radial compression, axial compression, torsion, and internal pressure, while studies on dry filament-wound structures have confirmed that void morphology and distribution are strongly linked to processing conditions [4], [8], [9].

A foundational understanding of how winding angles govern the elastic constants and nonlinear behavior of filament-wound tubes was largely established by the datasets of Soden et al. [10]. While these studies remain primary benchmarks, there is a need to improve upon this understanding from a microstructural standpoint. For instance, previous studies have shown that the response of filament-wound tubes depends strongly on the winding angle and loading mode. Tests performed on ring-shaped specimens extracted from filament wound tubes were found to exhibit pronounced winding-angle effects under tension and compression [8], while tests performed on full tubular specimens have examined axial compression, buckling, torsion, and multiaxial loading in carbon/epoxy wound structures [2], [6], [11]. However, these studies largely emphasize global structural response, buckling behavior, or post-failure assessment, with limited pre-test quantification of the as-manufactured microstructure in the specimens. Moreover, the available literature remains weighted toward pressure-vessel-dominant winding angles, whereas near-axial angles relevant to structures subjected to bending loads are much less comprehensively characterized [2], [7], [11].

Reviewed modeling literature have also shown recent numerical studies incorporated winding pattern, local interweaving regions, fiber-angle variation, and thickness variation into finite element descriptions of filament-wound cylinders [6], [8], [9]. However, most predictive approaches still rely on idealized or meso-smoothed architectures that are not calibrated against specimen-specific measurements of tow overlaps, intra-tow voids, and related process-induced features, although studies have suggested that strain in fiber crossover and undulation regions can be 1.07–1.13 times higher than in surrounding areas [12]. As a result, the connection between real as-manufactured tube microstructure and the measured deformation with the failure response of full cylindrical specimens remains insufficiently resolved [6], [8], [9].

While filament-wound composite tubes have been studied under axial loading, a clear specimen-specific correlation between as-manufactured microstructural features and the compressive response of full cylindrical towpreg-based carbon/epoxy tubes is still lacking. Crucially, a significant portion of the existing experimental literature relies on testing "cut-out" coupons or rings, which introduces edge effects and interrupts the continuous tow path [13], [14]. Moreover, near-axial winding angles (e.g., ±10°) remain sparsely studied relative to pressure-vessel-dominant angles, despite their relevance to several practical structures. This paper addresses these deficiencies through systematic microscopy-based characterization and axial compression testing of tow-based ±10° and ±45° filament wound tubes, providing the basis for broader characterization in the future that will include axial tension, torsion, and hoop-direction tension testing.

3. Mechanical and Experimental Setup

3.1. Material System and Tube Manufacturing Process

A towpreg system comprising a standard-modulus 12K carbon fiber tow reinforcement and an epoxy resin system with a nominal content of 30 ± 5 wt.% was used to manufacture 950 mm-long cylindrical tubes. The tows were wound on a 30 mm diameter mandrel using a custom filament winding system. The system utilized a closed-loop tension-controlled filament winding system, maintaining a tension tolerance of ±5 N. The nominal tow tension was maintained at ~30 N, while mandrel rotation speed varied depending on the winding angle. After winding, the tubes were wrapped with heat-shrink tape and cured in an oven. Based on the applied shrink-tape tension, tube diameter, tape width, and number of tape layers, the consolidation pressure during cure was estimated to be ~10 bar. Table 1 summarizes material and manufacturing details.

Two winding angles were considered in this study, namely ±10° and ±45°. A critical manufacturing observation was noted for the ±10° wound tubes where process-induced irregularities occurred near turnaround regions not observed in the ±45° specimens. These regions, which included tows sitting proud of the mandrel surface, were discarded post cure. While this manufacturing observation is qualitative, it highlights the increased propensity for microstructural variability in low-angle winding configurations in areas near the turn around regions.

Table 1. Material system and manufacturing details

Parameter	**Specification**
Reinforcement	Standard modulus 12K carbon fiber tow
Matrix	Epoxy resin system
Resin content	30 ± 5 wt.%
Cure cycle	Ramp to 120°C, hold for 5 hours, cool to minimum 60°C before removing from oven.
Winding platform	Custom closed-loop tension-controlled
Tension	~30 N

3.2. Sample preparation and optical microscopy

Cross-sectional and longitudinal-sectional samples for microscopic assessment were extracted from the manufactured tubes using a wet saw with a diamond blade. Sample preparation involved mounting, grinding, and polishing. Cold mounting was performed using a room-temperature curing resin system to avoid thermal disturbance of the epoxy matrix. The mounted samples were ground in several steps using SiC papers ranging from 180 to 1200 grit and subsequently polished using 3 μm and 1 μm diamond media to obtain a surface suitable for microscopy.

An opto-digital microscope, namely the VHX-5000 (Keyence), was used to assess the prepared samples. Qualitative assessment of the material microstructure and pre-existing local damage was coupled with quantitative assessment of void content, tow geometry, and fiber alignment. The software ImageJ and Python imaging were used to support quantitative assessment of void content. After generating binary images, void content was estimated from the segmented area fraction after visual comparison with the original images to ensure that the selected features corresponded to actual microstructural discontinuities rather than polishing artefacts. Representative original (microscopy) and binary images from a sample with ±45° winding angle are shown in Fig. 1.

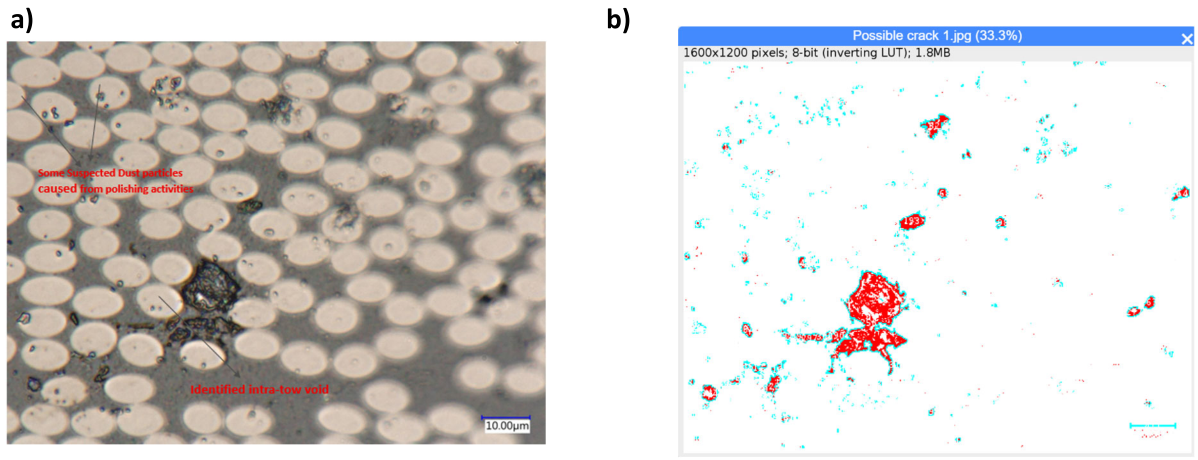

Fig. 1. Cross-sectional images of a ±45° filament wound tubular sample: a) original image obtained from microscopy, and b) generated binary image.

3.3. Test Specimen Preparation and Test Setup

Axial compression tests were performed on tubular specimens extracted from the manufactured tubes using a wet saw with a diamond blade (Table 2). Note, full tubular specimens were used instead of extracted coupons to preserve the continuous wound tow path and manufacturing-induced residual stresses, enabling characterization of the deformation response of the as-manufactured filament-wound material. Tubular end tabs were bonded to the specimens using the toughened epoxy adhesive 07333 (3M), where a custom alignment fixture was used to ensure concentricity between the specimen and end tabs. The external surface of each test specimen was prepared with a stochastic speckle pattern using matte-finish aerosol paints.

Table 2. Compression Specimen Geometry

Parameter	**±45° specimens**	**±10° specimens**
Outer diameter, OD	31 mm	31 mm
Inner diameter, ID	30 mm	30 mm
Wall thickness	0.5 mm	0.5 mm
Cross-sectional area	47.91 mm²	47.91 mm²
Gauge length	56–58 mm	60–70 mm

Axial compression tests were performed using a servo-hydraulic biaxial Instron 8800 test frame comprising a ±25 kN load cell operated in displacement control with a loading rate of 0.5 mm/min. Custom cup-shaped fixtures with an integrated locking assembly were used to grip the tubular specimens, where a flat stem on the fixtures enabled gripping by the hydraulic wedge grips on the test frame (Figure 2).

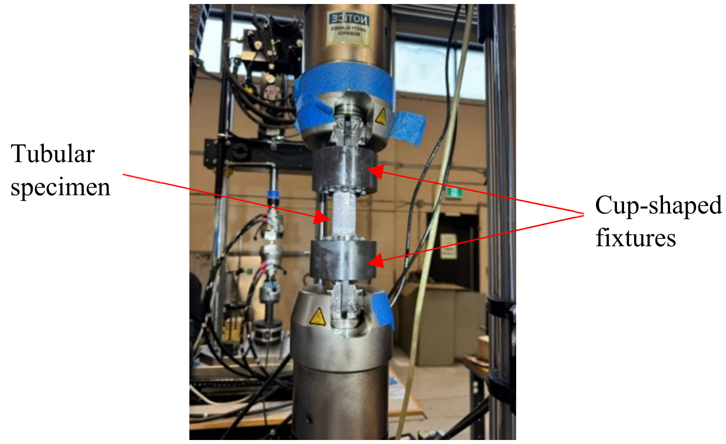

Fig. 2. Image of a speckled, tabbed tubular specimen gripped in custom cup-shaped fixtures and mounted onto the servo-hydraulic test frame.

3.4. Digital Image Correlation and Specimen Deformation

Full-field deformation of the test specimen gauge section was measured using an Aramis 3D stereo digital image correlation (DIC) system comprising two 5 MP cameras with F2.8/50mm lenses. The DIC system was used to evaluate axial strain and hoop strain and to monitor the radial displacement of the outer surface of the tubular specimens. The area of interest included the full gauge section on one half of the tubular specimens facing the cameras. The DIC field was discretized into approximately 9,000–9,600 facets, and the subset size used for the strain evaluation was 15 × 15 pixels^2. Based on the facet density, the effective spatial resolution was approximately 0.33 mm/pixel. Initially, images were captured using a two-phase sequence (i.e., 5 Hz followed by 0.5 Hz); however, for subsequent tests images were captured at a constant frequency of 1.8 Hz. Gaussian spatial filtering and short moving-window temporal averaging were applied to reduce measurement noise. These filtered fields were used to improve interpretability of deformation maps and enable capture of strain localization and damage onset.

The strain used to generate the stress–strain response was taken as the median axial strain over all valid facets within the area if interest as this approach captured the bulk deformation of the specimen. Radial displacement of the outer surface was also tracked to assess local wall buckling. Local buckling was considered absent when the radial displacement field did not form a broad symmetric out-of-plane mode along the specimen wall. It was imperative to ensure that damage onset occurred prior to specimen wall buckling as the material behavior was sought and not that of the tubular specimen. The primary fields captured were axial strain, transverse (hoop) strain, and out-of-plane (radial) displacement.

4. Results and Discussion

4.1. Microstructural characterization of ±45° and ±10° filament wound tube samples

Microscopy of ±45° filament wound samples showed that the as-manufactured architecture was generally well consolidated at the fiber scale. The void content for the assessed samples was measured to be <1% using ImageJ, revealing high overall quality. Microscopic assessment also revealed variation in the tow height and existence of resin-rich regions, which is indicative of non-uniform compaction (Figure 3). A localized intra-tow crack was observed in one of the samples, albeit this was a one-off occurrence and not representative of the bulk material. The measured tube wall thickness varied locally with an average of ~366 μm, while the tow pitch and width were ~327 μm and ~334 μm, respectively. The observed tow overlap or gap regions was typically on the order of 10–33 μm, revealing slight variability in the winding process. Moreover, the microscopic images analyzed were used to compute the misalignment of the fiber tows, with a preliminary misalignment estimate on the order of 2°.

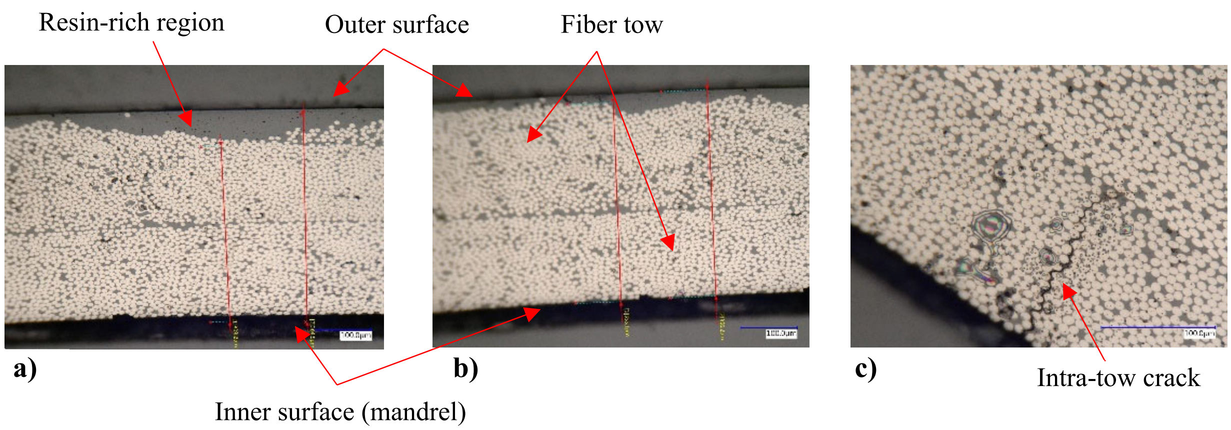

Fig. 3. Cross-sectional microscopic images of a ±45° wound sample: (a)-(b) through-thickness view showing non-uniform tow height, and (c) intra-tow crack.

Initial microscopic observations on ±10° tube filament wound samples (results not included herein) revealed similar features, including non-uniform tow height, resin-rich regions, and tow gaps/overlaps, as well as more extensive intra-tow cracking and near-surface defects for one sample. While these observations are currently qualitative and will be quantified in the next stage of the work, they are consistent with the manufacturing-related tow-placement irregularities for near-axial tow winding reported in previous work [15], [16].

4.2. Axial compressive response of the ±45° and ±10° wound specimens

The axial deformation response of the two tested ±45° wound tubular specimens was consistent in trend but differed in the extent of pre-damage accumulation and peak compressive resistance (Figure 4). The peak compressive stress for Specimens 1 and 2 were 79.94 MPa and 59.27 MPa, respectively, corresponding to an increase of approximately 35% for the former. Specimen 1 also exhibited a higher elastic modulus (Table 3). The Poisson's ratio for each specimen was greater than unity owing to the well-known shear-coupled or "scissor-like" deformation of ±45° wound tows under axial loading, which has been reported for angle-ply laminates [17]. The nonlinear deformation response of the two tested specimens also differed. For Specimen 2, the elastic limit and onset of strain localization were nearly coincident. By contrast, Specimen 1 exhibited elastic deformation followed by nonlinear deformation from 0.21% to 1.05% strain, prior to localization.

Full-field DIC of the ±45° wound specimens revealed the formation of a diagonal strain-localization band aligned with the tow orientation (Figure 5). Strain localization, which occurred prior to achieving a peak compressive stress, corresponds to the onset of local damage. For

Specimen 2, the first clear localized band was observed at an axial stress of 18.39 MPa, with damage onset visible on the specimen surface at this stage. For Specimen 1, the first strain localization band was observed at an axial stress of 67.59 MPa, where damage onset occurred thereafter. The captured radial displacement of the specimen outer surface (not included herein) did not reveal a broad symmetric out-of-plane deformation mode prior to the onset of localization, confirming that local buckling of the specimen walls did not precede strain localization.

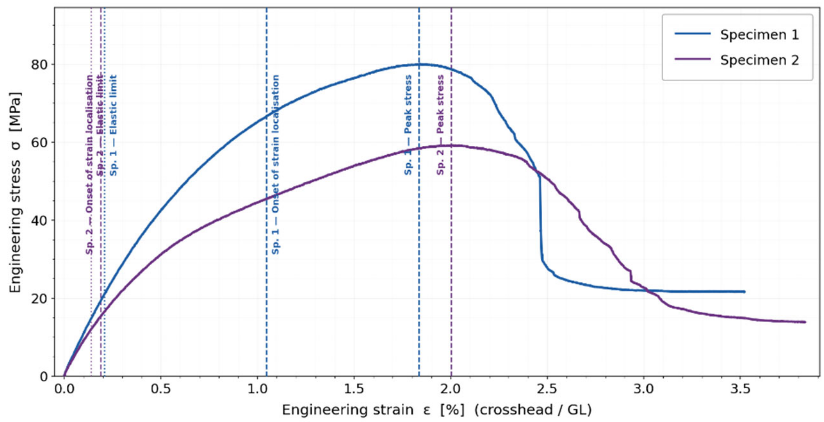

Fig. 4. Axial compressive stress-strain response for two tested ±45° wound tubular specimens.

Table 3. Mechanical properties of the ±45° specimens

Parameter	**Specimen 1**	**Specimen 2**
Elastic modulus, E_1 [GPa]	9.82	8.25
Peak compressive stress [MPa]	79.94	59.27
Strain at peak stress [%]	1.836	2.004
Poisson's ratio, ν_{12}	1.379	1.167

a)

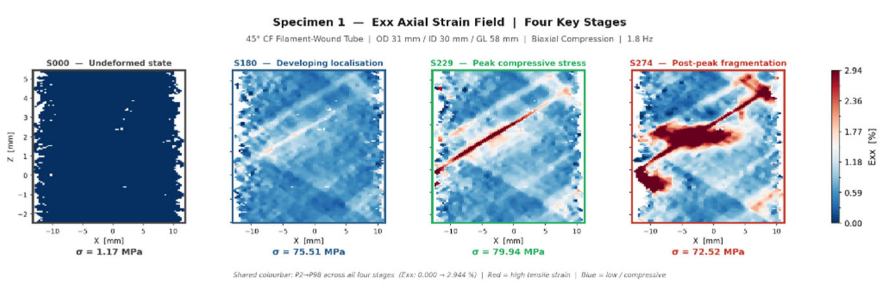

b)

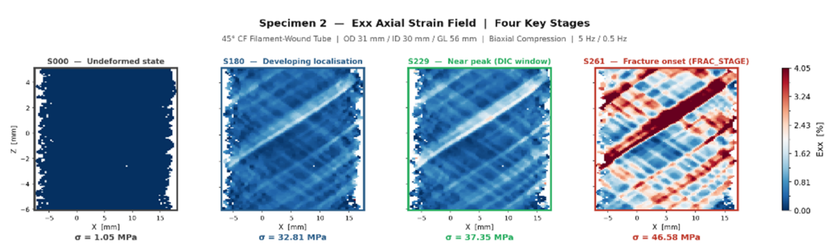

Fig. 5. Full-field axial strain contours for the ±45° wound specimens revealing strain localization: (a) Specimen 1, and (b) Specimen 2.

In contrast to the ±45° filament wound specimens, the tested ±10° filament wound specimen exhibited a substantially higher peak compressive stress of 108.28 MPa (Fig. 6), reflecting the greater contribution of fibers aligned closer to the loading direction. The stress-strain response was characterized by an initial elastic response followed by damage onset (confirmed by strain localization captured by DIC) and a progressive damage plateau, during which the stress fluctuated in the range 80–108 MPa, indicating repeated local micro-cracking and load redistribution prior to final fracture. Interestingly, damage initiated at a strain magnitude similar to that of the ±45° filament wound specimens. Although final failure occurred after continued damage accumulation rather than immediate localization at onset, further assessment of damage progression is required to confirm the governing damage mechanisms.

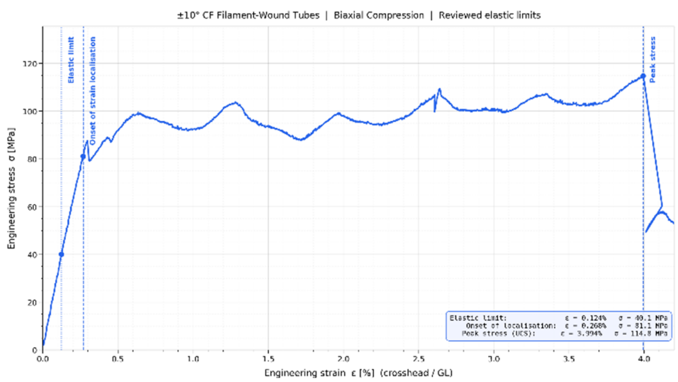

Fig. 6. Axial compressive stress-strain response for a ±10° wound tubular specimen.

4.3. General discussion

The axial compressive response of the two tested ±45° wound specimens were not consistent, despite having the same nominal winding angle and similar overall geometry. One tubular specimen exhibited a higher modulus, higher peak compressive stress, and a more extended nonlinear regime before strain localization, whereas the second specimen exhibited localization much earlier and abruptly. Currently, the most consistent interpretation is that specimen-to-specimen variation in local tow geometry and compaction (i.e., fiber volume faction) contributed to the observed difference in compressive response. The microscopy results suggest that the most relevant microstructural features are the local tow-scale geometric irregularities, including overlap or gap regions and associated matrix-rich zones. These features provide plausible sites for local stress concentration and earlier damage initiation under axial compression. Given the low estimated void content in the assessed samples, voids are not deemed to contribute substantially to the axial compressive response of the specimens.

Preliminary mechanical results for the ±10° wound specimens reveal a distinctly different compressive response from the ±45° wound specimens, consistent with the change in winding angle and the increased influence of fibre-dominated load transfer in the near-axial architecture. In addition, preliminary microscopy observations indicate that the ±10° wound samples contain more pronounced local irregularities, including nonuniform tow height and intra-tow cracks. Once additional ±10° wound samples are investigated, a more direct basis for linking the winding angle and resulting material structure to the compressive deformation and damage development will be established.

5. Conclusions

This study investigated the relationship between microstructure and axial compressive response of towpreg-based ±45° and ±10° filament-wound carbon fiber/epoxy tubes through microscopy and compression testing. The estimated void content in the assessed ±45° wound samples was <1%, while tow-scale geometric variations such as nonuniform height, overlap/gap regions, and resin-rich regions were observed. The two tested ±45° specimens exhibited a similar overall axial compression deformation response but differed in stiffness, peak compressive stress, and the extent of nonlinear deformation prior to strain localization. Full-field strain measurements further showed that damage initiated as a narrow band aligned with the wound architecture before peak stress and without evidence of local wall buckling. These results provide an initial process-structure-property relationship for filament-wound composite tubes. Ongoing work includes further microstructure assessment and compression testing of ±10° tubes as well as for tubes with additional winding angles. Also, tension, torsion, and hoop-direction testing will be performed to support a broader process–structure–property characterization and the long-term goal of developing high-fidelity micromechanics-based predictive models.

6. References

[1] M. J. Donough, Shafaq, N. A. St John, A. W. Philips, and B. Gangadhara Prusty, "Process modelling of In-situ consolidated thermoplastic composite by automated fibre placement – A review," *Compos. Part A Appl. Sci. Manuf.*, vol. 163, p. 107179, Dec. 2022, doi: 10.1016/J.COMPOSITESA.2022.107179.

[2] Y. Chang, W. Wen, Y. Xu, H. Cui, and Y. Xu, "Quasi-static mechanical behavior of filament wound composite thin-walled tubes: Tension, torsion, and multi-axial loading," *Thin-Walled Structures*, vol. 177, p. 109361, Aug. 2022, doi: 10.1016/J.TWS.2022.109361.

[3] K. C. Jois, T. Mölling, J. Schuster, N. Grigat, and T. Gries, "Towpreg manufacturing and characterization for filament winding application," *Polym. Compos.*, vol. 45, no. 9, pp. 7893–7905, Jun. 2024, doi: 10.1002/PC.28311;REQUESTEDJOURNAL:JOURNAL:15480569;WGROUP:STRING:PUBLICATION.

[4] M. Ueda *et al.*, "Voids in type-IV composite pressure vessels manufactured by a dry filament-winding process," *International Journal of Pressure Vessels and Piping*, vol. 208, p. 105154, Apr. 2024, doi: 10.1016/J.IJPVP.2024.105154.

[5] A. J. Eko, J. Epaarachchi, J. Jewewantha, and X. Zeng, "A review of type IV composite overwrapped pressure vessels," *Int. J. Hydrogen Energy*, vol. 109, pp. 551–573, Mar. 2025, doi: 10.1016/J.IJHYDENE.2025.02.108.

[6] T. V. Lisbôa, J. H. S. Almeida, A. Spickenheuer, M. Stommel, S. C. Amico, and R. J. Marczak, "FEM updating for damage modeling of composite cylinders under radial compression considering the winding pattern," *Thin-Walled Structures*, vol. 173, p. 108954, Apr. 2022, doi: 10.1016/J.TWS.2022.108954.

[7] F. Eggers, J. H. S. Almeida, C. B. Azevedo, and S. C. Amico, "Mechanical response of filament wound composite rings under tension and compression,"

Polym. Test., vol. 78, p. 105951, Sep. 2019, doi: 10.1016/J.POLYMERTESTING.2019.105951.

[8] S. Duda *et al.*, "Experimental characterization and modeling of cylindrical CFRP structures under quasi-static multiaxial loading conditions," *Thin-Walled Structures*, vol. 195, p. 111364, Feb. 2024, doi: 10.1016/J.TWS.2023.111364.

[9] E. A. W. de Menezes, T. V. Lisbôa, J. H. S. Almeida, A. Spickenheuer, S. C. Amico, and R. J. Marczak, "On the winding pattern influence for filament wound cylinders under axial compression, torsion, and internal pressure loads," *Thin-Walled Structures*, vol. 191, p. 111041, Oct. 2023, doi: 10.1016/J.TWS.2023.111041.

[10] P. D. Soden, M. J. Hinton, and A. S. Kaddour, "Lamina properties, lay-up configurations and loading conditions for a range of fibre reinforced composite laminates," *Failure Criteria in Fibre-Reinforced-Polymer Composites*, pp. 30–51, Jan. 2004, doi: 10.1016/B978-008044475-8/50003-2.

[11] J. H. S. Almeida *et al.*, "Design, modeling, optimization, manufacturing and testing of variable-angle filament-wound cylinders," *Compos. B Eng.*, vol. 225, p. 109224, Nov. 2021, doi: 10.1016/J.COMPOSITESB.2021.109224.

[12] C. Shen and X. Han, "Damage and failure analysis of filament wound composite structure considering fibre crossover and undulation," *Advanced Composites Letters*, vol. 27, no. 2, pp. 55–70, Mar. 2018, doi: 10.1177/096369351802700202;SUBPAGE:STRING:FULL.

[13] A. Kastenmeier and V. Schmid, "Specimen Preparation and Material Characterization of Filament Wound Composite Tubes," 2017.

[14] H. Rigneault *et al.*, "Mechanical characterization of composite materials from curved structures," *Focus on Microscopy*, no. 1, p. 255, Jun. 2016, doi: 10.34894/VQ1DJA.

[15] E. Natale, A. Gaspari, L. Chiominto, G. D'Emilia, and A. G. Stamopoulos, "Morphological analysis of as-manufactured filament wound composite cylinders using contact and non-contact inspection methods," *Eng. Fail. Anal.*, vol. 158, p. 108011, Apr. 2024, doi: 10.1016/J.ENGFAILANAL.2024.108011.

[16] C. Hopmann, N. Magura, R. Müller, D. Schneider, and K. Fischer, "Impact of winding parameters on the fiber bandwidth in the cylindrical area of a hydrogen pressure vessel for generating a digital twin," *Polym. Compos.*, vol. 43, no. 3, pp. 1577–1589, Mar. 2022, doi: 10.1002/PC.26479;REQUESTEDJOURNAL:JOURNAL:15480569;WGROUP:STRING:PUBLICATION.

[17] J. H. S. Almeida, M. L. P. Tonatto, M. L. Ribeiro, V. Tita, and S. C. Amico, "Buckling and post-buckling of filament wound composite tubes under axial compression: Linear, nonlinear, damage and experimental analyses," *Compos. B Eng.*, vol. 149, pp. 227–239, Sep. 2018, doi: 10.1016/J.COMPOSITESB.2018.05.004.